


## Article

# Experimental Study on the Thermal Performance of 3D-Printed Enclosing Structures

Darya Nemova , Evgeny Kotov, Darya Andreeva, Svyatoslav Khorobrov, Vyacheslav Olshevskiy, Irina Vasileva, Daria Zaborova and Tatiana Musorina

Peter the Great St. Petersburg Polytechnic University, 195251 St. Petersburg, Russia; ekotov.cfd@gmail.com (E.K.); tarasovads@gmail.com (D.A.); svyatoslav.khorobrov@gmail.com (S.K.); volshevskiy@yandex.ru (V.O.); iravassilek@mail.ru (I.V.); zaborova\_dd@spbstu.ru (D.Z.); tamusorina@mail.ru (T.M.)

\* Correspondence: nemova\_dv@spbstu.ru

**Abstract:** Three-dimensional printing, or additive manufacturing, is one of the modern techniques emerging in the construction industry. Three-Dimensional Printed Concrete (3DPC) technology is currently evolving with high demand amongst researchers, and the integration of modular building systems with this technology would provide a sustainable solution to modern construction challenges. This work investigates and develops energy-efficient 3D-printable walls that can be implemented worldwide through energy efficiency and sustainability criteria. Numerical research and experimental investigations, bench tests with software packages, and high-precision modern equipment have been used to investigate the thermal performance of 3DPC envelopes with different types of configurations, arrangements of materials, and types of insulation. The research findings showed that an innovative energy-efficient ventilated 3DPC envelope with a low thermal conductivity coefficient was developed following the climatic zone. The annual costs of heat energy consumed for heating and carbon footprint were determined in the software package Revit Insight to assess the energy efficiency of the 3D-printed building. The thermal properties of the main wall body of the tested 3D-printed walls were calculated with on-site monitoring data. The infrared thermography technique detected heterogeneous and non-uniform temperature distributions on the exterior wall surface of the 3DPC tested envelopes.

**Keywords:** building; energy efficiency; energy-efficient buildings; 3D printing; high-performance building envelope; additive technology for energy-efficient buildings



**Citation:** Nemova, D.; Kotov, E.; Andreeva, D.; Khorobrov, S.; Olshevskiy, V.; Vasileva, I.; Zaborova, D.; Musorina, T. Experimental Study on the Thermal Performance of 3D-Printed Enclosing Structures. *Energies* **2022**, *15*, 4230. <https://doi.org/10.3390/en15124230>

Academic Editor: Izabela Hager

Received: 4 April 2022

Accepted: 6 June 2022

Published: 8 June 2022

**Publisher's Note:** MDPI stays neutral with regard to jurisdictional claims in published maps and institutional affiliations.



**Copyright:** © 2022 by the authors. Licensee MDPI, Basel, Switzerland. This article is an open access article distributed under the terms and conditions of the Creative Commons Attribution (CC BY) license (<https://creativecommons.org/licenses/by/4.0/>).

## 1. Introduction

### 1.1. 3D Printing

Three-dimensional printing, or additive manufacturing, is one of the modern techniques emerging in the construction industry. It is characterized by a fast and low-cost building process. Three-Dimensional Printed Concrete (3DPC) technology is currently evolving with high demand amongst researchers. Integrating a modular building system with this technology would provide a sustainable solution to modern construction challenges.

Additive manufacturing, which allows for rapid prototyping and so-called on-demand manufacturing, has become a common method of creating parts or entire devices. On a 3D printer, the real objects are created layer by layer, which creates extraordinary opportunities for a variety of applications for devices of this type. With the help of 3D printing, objects can be made in almost any shape. Three-dimensional printing opens up a wide range of possibilities for architects and engineers. However, it is unclear whether this solution is safe enough to be used without restrictions, wherever and by whomever it is. Thus, the presented publication contains information about additive manufacturing, various technologies, and printing methods using a variety of raw materials. It provides an overview of publications over the past five years devoted to 3D printing, especially with

regard to the potential release of chemicals and particles as a result of the use of such printers in the workplace and private premises.

### 1.2. 3D Printing Building Energy Efficiency

Different wall configurations for 3D printing using different materials have been designed to reduce the U-shaped values of printed walls in accordance with the rules of climatic zones. As a result of the simulation, the minimum value of heat transmission is  $0.15 \text{ W/m}^2\cdot\text{K}$ . The results show that in order to achieve the necessary U-values and design characteristics, it is necessary to maintain a balance between the cavities and the 3D printing material. In search of the best results to achieve this balance, several series of configurations have been introduced. Finally, in order to study the impact of climatic conditions on the 3D-printed environment, the annual energy demand for each climate zone was estimated.

This study examines the fire performance characteristics of 20 numbers with different 3D wall configurations using finite element models under standard fire conditions. The analysis of fire performance characteristics showed that the curtain walls of the 3DPC cavity have significant resistance under standard fire load, and their characteristics can be further improved with the help of stone wool insulation [1].

Due to hybridization and integration with other energy-efficient technologies, 3DPC demonstrates promising opportunities for reducing energy consumption and increasing thermal comfort in the room [2,3]. However, detailed studies of the thermal aspects of 3DPC are currently very limited. Robati et al. [4] investigated the effect of a mixture of 3DPC structures on thermal characteristics. It was found that the concrete mixture's composition strongly affects its thermal characteristics, especially due to changes in the density of the aggregate and the proportion of the material. Prasittisopin conducted two studies to study the thermal insulation characteristics of wall panels printed on a 3D printer, prepared with different surface textures and building mixes [5]. It was found that panels printed on a 3D printer act as a heat buffer, and their thermal insulation characteristics directly depend on the density of the 3D printing solution. A panel printed on a 3D printer from a low-strength solution corresponding to a lower density demonstrates the best thermal insulation characteristics.

The introduction of mandatory energy efficiency standards for new buildings is one of the most cost-effective ways to ensure energy conservation in the residential sector. Standards must be mandatorily updated and take into account territorial and climatic features to have an effect. The existing norms do not contain methods for conducting thermomechanical calculations of 3D printed structures. The norms do not allow for correctly assessing the structures' thermal heterogeneity, the influence of configuration, materials, insulation, heat-conducting inclusions, and the sequence of layers during printing [6–8].

The topic of the energy efficiency of enclosing structures was touched upon in studies [8–14]. After analyzing the research, it can be concluded that the main disadvantages of studying 3D printed construction technology are shortcomings in the field of studying the energy efficiency of such structures and the lack of a methodology for their thermal calculation [1,6,14–27].

Some researchers have tried to adjust the thermal characteristics of 3DPC using topology optimization. Lowke et al. [28] indicated that introducing cavities in areas requiring low thermal conductivity can improve insulation properties. The proposed approach makes it possible to combine zones with different thermal characteristics into structural bodies printed on a 3D printer. It is important to assess the topology optimization and energy efficiency of enclosing structures using numerical modeling [29,30]. Buswell et al. [31,32] tried to minimize the path of thermal conductivity in 3D printed wall elements. They produced two wall panels with the same external geometry but with different internal cross-sections of the print for comparison. The result showed opportunities to improve the thermal resistance characteristics by optimizing the topology. While previous studies have conducted some studies of the thermal characteristics of 3D printed components, taking



into account materials and geometric aspects, studies on the thermal characteristics of an entire 3DPC building have not yet been conducted.

In the works presented above, there are no studies with the simultaneous execution of a mathematical model and a physical experiment on a real model for comparison. In addition, an analysis of the literature showed that in the works there is no assessment of the consumed thermal energy when using additive walls with one or another filling and with one or another internal configuration.

### 1.3. Aim and Tasks

This research aimed to determine the suitability and the energy efficiency of 3D-printed enclosing structures and establish the optimal configuration for obtaining enclosing structures with the best characteristics.

The main tasks were as follows:

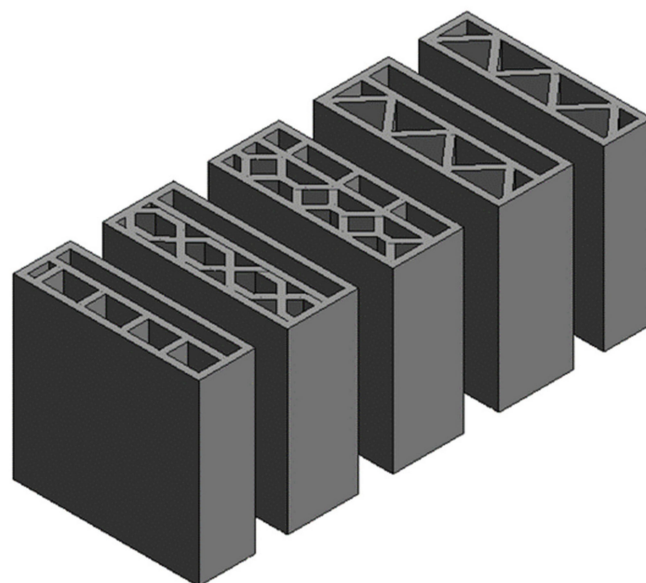
1. The evaluation of the thermal resistance coefficient of structures obtained using 3D printing;
2. The creation of a mathematical model to describe the process of heat and mass transfer;
3. The development and implementation of an experimental bench for validating the proposed mathematical model.

## 2. Materials and Methods

### 2.1. Problem Statement

The research objective was to determine the heat transfer resistance of the enclosing structures obtained by the additive method. The heat transfer resistance could be determined by mathematical modeling since it is possible to more accurately estimate the integral characteristics (averaged heat flux over the surface, etc.) than in an experiment, where it is possible only to determine these values at monitoring points. The correctness of the description of the heat and mass transfer process by the mathematical model was validated by comparing experimental results.

For numerical study, several structures were selected that differed from each other in the internal structure of the cavities but were similar in form factor. These designs are the most typical for practical applications. Except for the structures' depths, the tested samples' linear dimensions remained the same for all samples (Figure 1).



**Figure 1.** Types of enclosing structures.

The construction was chosen based on preliminary numerical studies, which were subsequently used to conduct a physical experiment).

## 2.2. Experimental Setup

The following test equipment was used for the experimental study of the thermal properties of the additive panel:

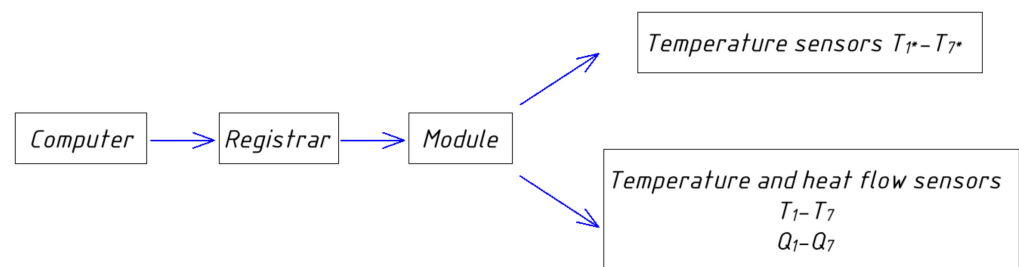
1. Climatic chamber No. 1;
2. Climatic chamber No. 2;
3. The flux density and temperature meter (The technical characteristics are presented in Table 1).

**Table 1.** The technical characteristics of the heat flux density and temperature meter.

| Characteristic  | Value                           |
|---|---------------------------------|
| Measuring the range of heat flux density, $W/m^2$   | 10–500                          |
| Temperature measurement ranges, $^{\circ}C$   | $-40^{\circ}C$ – $+70^{\circ}C$ |
| Limits of the permissible basic relative error of measuring the heat flux density, %, no more | $\pm 6$                         |
| Limits of the permissible basic absolute error of temperature measurement, $^{\circ}C$        | $\pm 0.2$                       |

The supported temperature range was from  $-70^{\circ}C$  to  $+100^{\circ}C$  for climatic chamber No. 1. A two-stage air-cooled refrigerating machine created cooling in climate chamber No. 1. The supported temperature ranged from  $-70^{\circ}C$  to  $+180^{\circ}C$  for climatic chamber No. 2.

The device consists of a registrar, a module, temperature and heat flow sensors, and connecting cables. Schematically, the principle of operation is shown in Figure 2.



**Figure 2.** Schematic diagram of the device operation ( $T_1$ – $T_7$  are temperature measurement sensors,  $Q_1$ – $Q_7$  are flow measurement sensors,  $T_{1*}$ – $T_{7*}$  are additional sensors for temperature measurement).

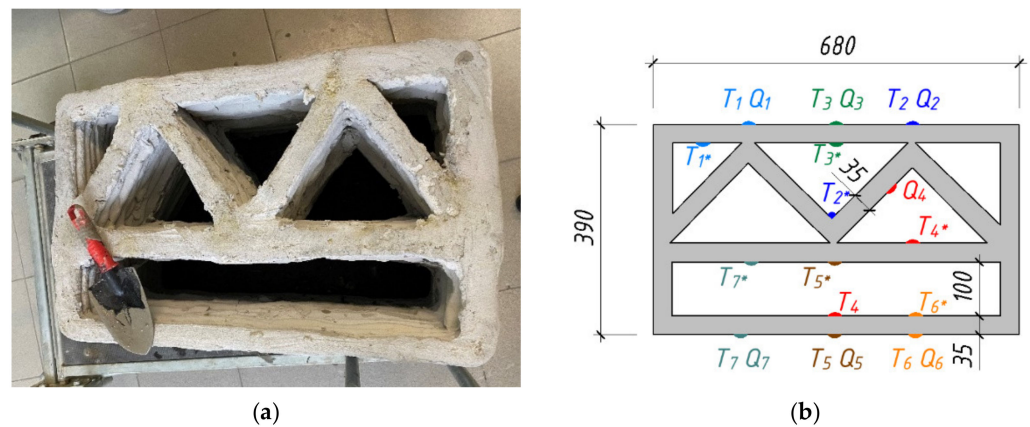
The wall panel size made by the additive method was  $390\text{ mm} \times 680\text{ mm} \times 310\text{ mm}$ . The wall thickness of the structure was 35 mm.

For the manufacture of the panel, a dry mix was used, in which the maximum size of the aggregate fraction was 0.63 mm. A total of 1800 kg of dry mix was needed to prepare  $1\text{ m}^3$  of the structure. Water consumption for mixing 1 kg of dry mix was 0.13–0.16 L.

The mixture used after hardening had the following properties:

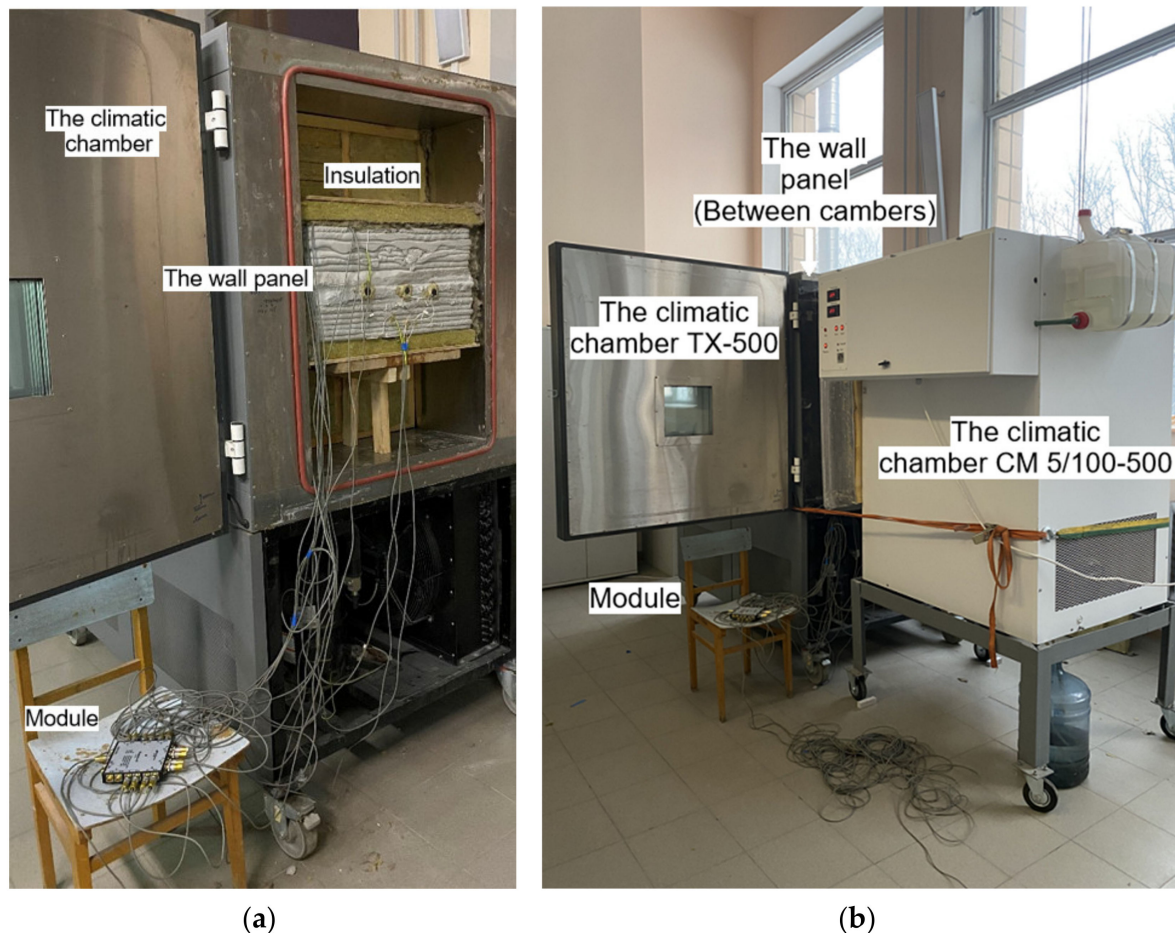
1. Compressive strength after 24 h was min 18 MPa;
2. Compressive strength after 28 days was min 40 MPa;
3. Bending tensile strength after 24 h was min 4 MPa;
4. Tensile strength in bending after 28 days was min 8 MPa;
5. Waterproof mark was min W14;
6. Mark on frost resistance was F600;
7. Modulus of elasticity was 26 GPa;
8. Climatic zones of application—all zones.

Figure 3a shows the type of construction. The temperature and heat flow sensors were evenly located on the panel surface (Figure 3b).



**Figure 3.** (a) Wall panel; (b) Sensor layout.

The tested sample of a wall panel made in an additive way had a smaller size than the inner part of the climate chamber. The remaining space was hermetically filled with insulation. The general view of the stand with the test sample is shown in Figure 4.



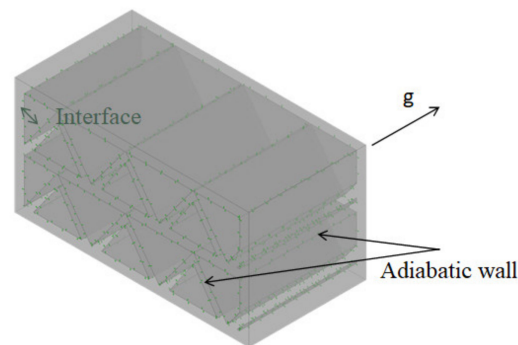
**Figure 4.** Stand with the additive wall panel. (a) The sample is placed in a climate chamber No. 1.; (b) The sample is placed between two climatic chambers, the start of testing.

The temperature in climatic chamber No. 1 was set to  $-24\text{ }^{\circ}\text{C}$ . Climatic chamber No. 2 was set to  $+22\text{ }^{\circ}\text{C}$ .

The heat flux density and temperature meter was programmed to measure temperature and heat flow during the day and record values every 15 min.

### 2.3. Numerical Simulation of Heat and Mass Transfer in Enclosing Structures Created by the Method of Additive Technologies

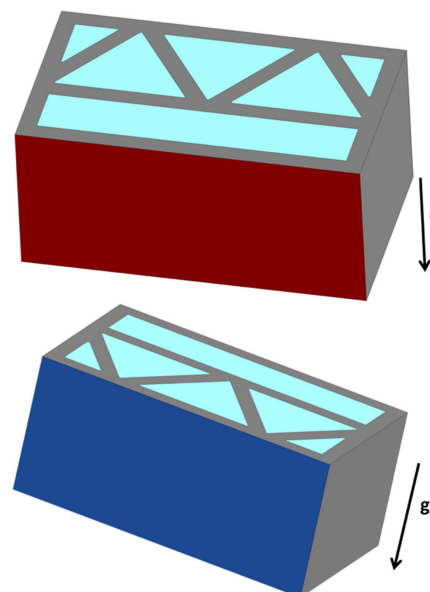
The description of the heat and mass transfer process in block enclosing structures created by the additive method implies the description of two methods of heat transfer: heat conduction and convection. The solution to this problem was carried out in the ANSYS CFX software package. The finite volume method was employed to carry out the calculation. A hybrid mesh with a total of 4.9 million nodes and 4.5 million cells was used. The problem was solved in a stationary setting. For cavities filled with air, a perfect gas with a known density was used as a model of the medium. The airflow was described in a laminar formulation using the Boussinesq approximation. Figure 5 shows the boundary conditions.



**Figure 5.** Boundary conditions.

On the outer boundaries of the block, the third kind of condition was set, convective temperature described by the Newton–Richmann law. The heat transfer coefficient values were calculated from the approximation for convection near a vertical plate (Churchill and Chu approximation). The value of the convective temperature was taken equal to 22 °C inside the room and −24 °C outside. At the border of two different materials (concrete–air, concrete–insulation), the condition for the conservation of energy was set (equality of temperatures and heat fluxes).

There were 4 general boundary conditions: adiabatic wall for concrete (gray color in Figure 6) and for air domains (light blue color in Figure 6; adiabatic wall condition was Neumann boundary condition with zero heat flux), hot wall (red color at Figure 6, Dirichlet boundary condition for temperature equal to 20 °C), and cold wall (blue color at Figure 6, Dirichlet boundary condition for temperature equal to −22 °C).



**Figure 6.** Boundary conditions by colors and gravity direction.

The air domain was set to have the buoyancy to take natural convection into account. The gravity vector direction is shown in Figure 6. Air density was calculated according to the ideal gas equation of state. All thermal properties of materials are shown in Table 2. The calculation was made in the assumption of laminar convection, so no turbulence models were used.

**Table 2.** Thermal properties of used materials.

|          | Density           | Viscosity                  | Specific Heat  | Thermal Conductivity | Molar Mass |
|----------|-------------------|----------------------------|----------------|----------------------|------------|
| Air      | kg/m <sup>3</sup> | Pa·s                       | J/(kg·K)       | W/(m·K)              | g/mol      |
| Concrete | ideal gas<br>1900 | $1.83 \times 10^{-5}$<br>- | 1004.4<br>1130 | 0.0261<br>0.7        | 28.96<br>- |

### 3. Results and Discussion

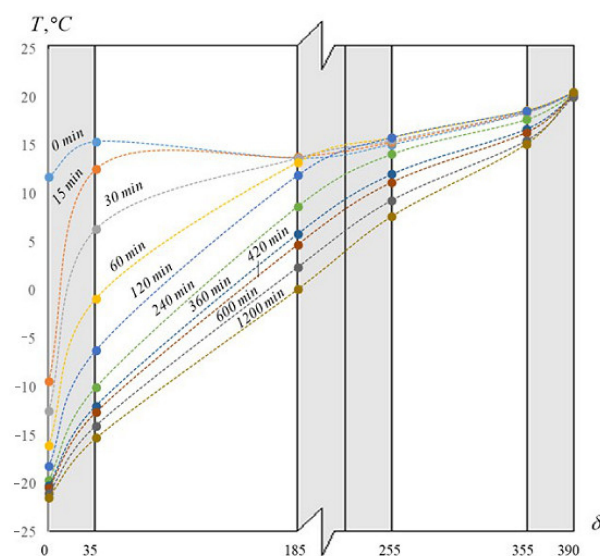
#### 3.1. Verification and Validation of CFD Simulations

The validation and verification of the proposed CFD model are carried out by comparing the results obtained numerically and at the experimental stand. The results are compared by comparing such physical quantities as temperature and heat flow at the monitoring points (Figure 4b). After evaluating the reliability of the proposed CFD model, one can evaluate the reliability of the integral characteristics obtained with its help, such as the coefficient of heat transfer resistance.

##### 3.1.1. Experimental Results

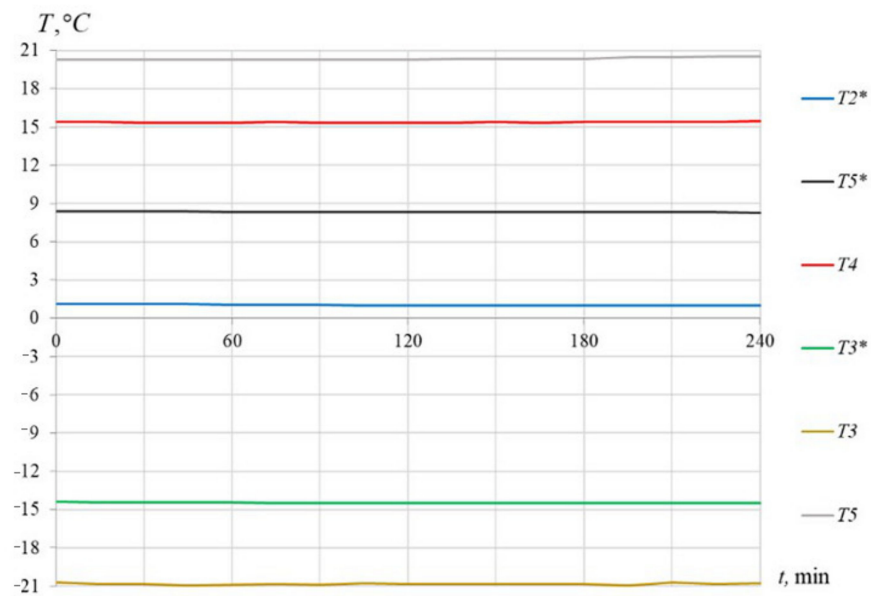
The time of temperature drop in the experimental sample of 3D-printed enclosing structure (Section 1.1) was evaluated: temperature sensors were located on each surface of the sample (Figure 3), which made it possible to evaluate the temperature profile.

The experimental sample of 3D-printed enclosing structure was placed for a day in two climatic chambers with different temperatures,  $T_{cold} = -24\text{ }^{\circ}\text{C}$  (temperature in a cold chamber) and  $T_{hot} = +22\text{ }^{\circ}\text{C}$  (temperature in a warm chamber), to assess the distribution of the temperature profile over the thickness ( $\delta$ ) of the structure. The isotherm ( $t = 0\text{ min}$ ) showed the initial temperature distribution in the sample. In the cold chamber, the temperature  $T_{cold} = -24\text{ }^{\circ}\text{C}$  was dialed within 40 min. For the first time within 120 min, there was a precipitate drop in the temperature at the sides  $\delta = 0\text{ mm}$  and  $\delta = 35\text{ mm}$ . The temperature drop occurred mainly inside the structure ( $\delta = 185\text{ mm}$ ,  $\delta = 255\text{ mm}$ ). After that, the time interval for comparing isotherms was more than two hours. The distributions of isotherms for the first day of the experiment are shown in Figures 7 and 8.



**Figure 7.** Change of isotherms in time to a stationary state.





**Figure 8.** Steady state of isotherms.

Figure 8 shows the size of the wall and isotherms at key points in the sample of structures in the chamber during the experiment. The temperature at key points of the structure took a constant value for 240 min.

The stationary state of the structure was achieved after 1200 min.

### 3.1.2. Estimating Experimental Errors

The repeatability of the experiments was three times. The temperatures were taken in the steady-state mode for each sensor for three experiments to calculate the experiments' accuracy.

The standard deviation for each test point is calculated using the following formula:

$$s = \sqrt{\frac{\sum_{i=1}^n (x_i - x_{avg})^2}{n - 1}} \quad (1)$$

$x_i$  is the value of a single sample value (experimental temperature);  $x_{avg}$  is the arithmetic mean of the sample:

$$x_{cp} = \frac{x_1 + x_2 + x_3}{3} \quad (2)$$

$x_i$  is the value of a single sample value (experimental temperature);  $x_{avg}$  is the average of the sample;  $x_{avg} = (x_1 + x_2 + x_3)/3$ ,  $n$  is the number of items in the selection.

Then the coefficient of variation (relative standard deviation) is as follows:

$$c_v = \frac{s}{x_{avg}} \cdot 100\% \quad (3)$$

The arithmetic means for the first point (according to Formula (2)) are:  $x_{cp} = \frac{x_1 + x_2 + x_3}{3} = \frac{20.84 + 20.34 + 20.48}{3} = 20.59^\circ\text{C}$ .

The standard deviation (according to Formula (1)) is:

$$s = \sqrt{\frac{\sum_{i=1}^n (20.48 - 20.59)^2 + (20.34 - 20.59)^2 + (20.84 - 20.59)^2}{2}} = 0.2579^\circ\text{C}$$

The coefficient of variation (according to Formula (3)) is

$$c_v = \frac{0.2579}{20.59} \cdot 100\% = 1.25\%$$

The relative standard deviation did not exceed 3% for carrying out the experiment, which corresponds to the average degree of data dispersion (from 10% to 20%).

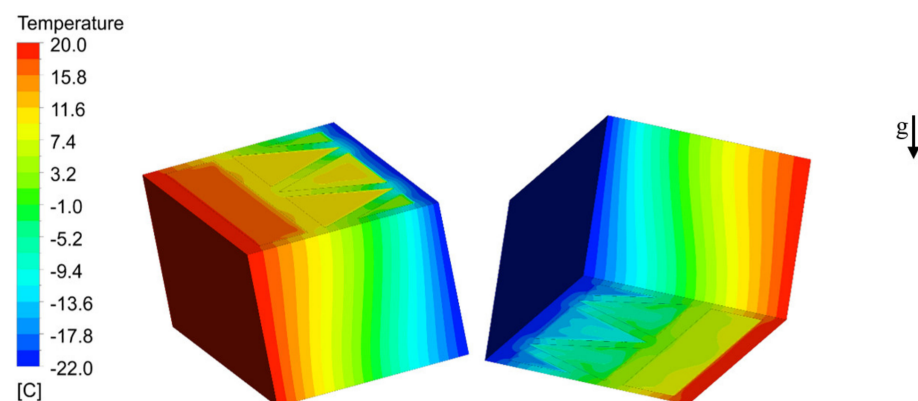
Table 3 presents the data of average values and experimental accuracy.

**Table 3.** Average values and errors.

| <i>n</i> | The Temperature in Steady-State Mode |        |        | Average Value | Standard Deviation | Error |
|----------|--------------------------------------|--------|--------|---------------|--------------------|-------|
|          | Day 1                                | Day 2  | Day 3  |               |                    |       |
| T3       | −20.84                               | −20.34 | −20.48 | −20.59        | 0.2579             | 1.25% |
| T3*      | −14.48                               | −14.3  | −14.6  | −14.39        | 0.1510             | 1.05% |
| T2*      | 1.04                                 | 1.04   | 1.05   | 1.04          | 0.0058             | 0.56% |
| T5*      | 8.33                                 | 8.58   | 8.32   | 8.455         | 0.1468             | 1.74% |
| T4       | 15.37                                | 15.04  | 14.81  | 15.205        | 0.2793             | 1.84% |
| T5       | 20.35                                | 20.45  | 20.41  | 20.4          | 0.0501             | 0.25% |

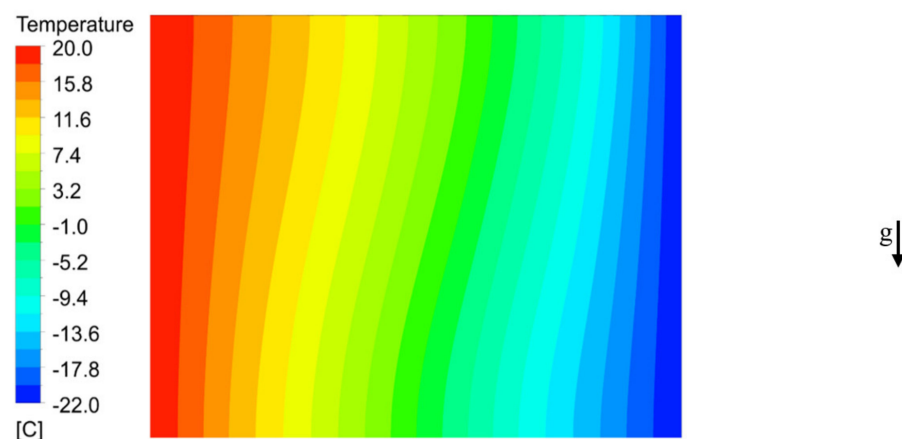
### 3.1.3. CFD Modeling of the Basic Construction

First of all, the temperature field of the construction is considered (Figure 9). Air is hotter on the upper part of the construction than the concrete lintel in the middle, but on the lower part, the air is colder than the lintel. The local temperature difference between concrete and air is around 15 °C.



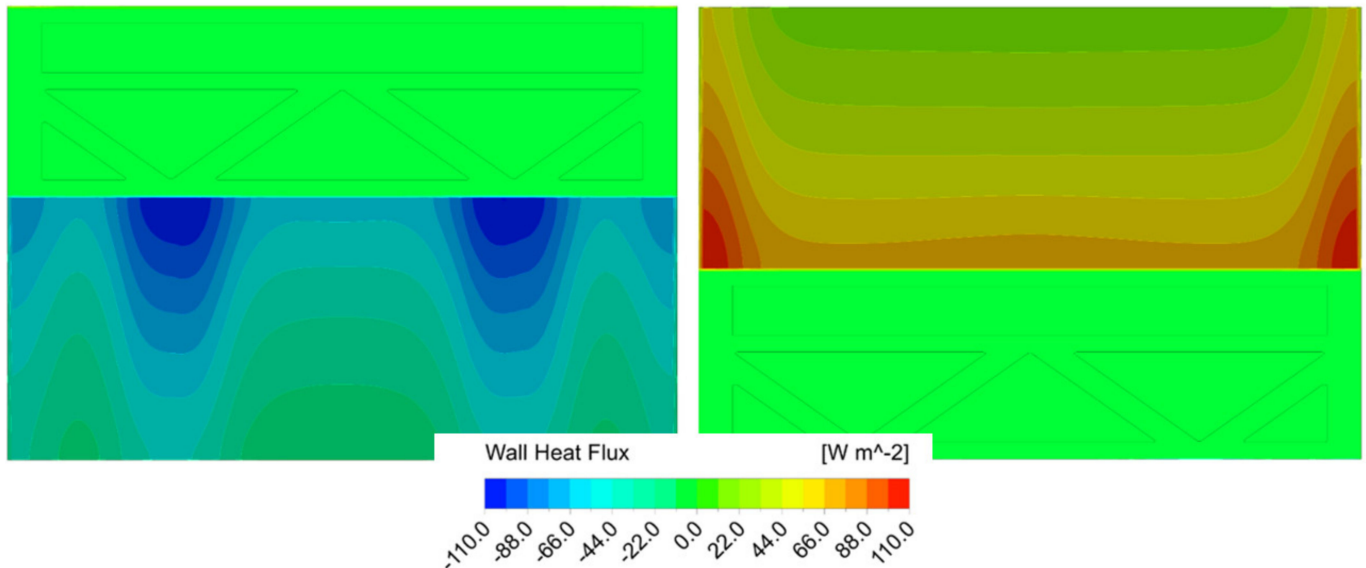
**Figure 9.** Temperature field on the construction.

Convection effects are most noticeable on the construction's side (Figure 10). The temperature isoline becomes more curved while moving the construction's center from either the hot or cold side. The temperature difference between the lower and the upper sides in the center of the object's side face is about 5 °C.



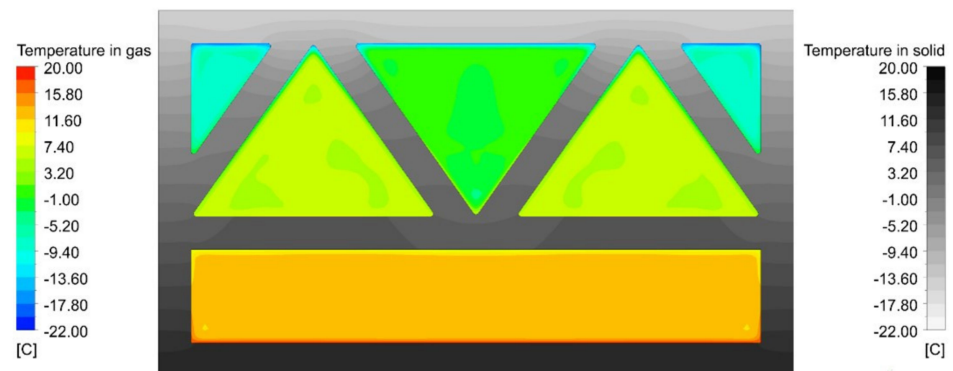
**Figure 10.** Temperature field on the side of the construction.

Figure 10 shows the heat flux through the construction. The heat flux through solid parts is severely higher (up to  $2\times$ ) than the heat flux through the air. Convection also influences heat flux distribution on surfaces. As temperature gradients change because of convection (as shown in Figure 9), heat flux changes (from 100 to  $70\text{ W/m}^2$ ) along the vertical coordinate (Figure 11).



**Figure 11.** Wall heat flux through the construction.

As all thermal characteristics change along with vertical coordinates because of natural convection, it is possible to take the middle cross-section plane to obtain an average change in values through the construction (Figure 12).



**Figure 12.** Temperature field on the middle cross-section plane of the construction.

There is one rectangular cavity, two hot triangle cavities, and three cold rectangular cavities. All cavities except small triangle ones seem to have stabilizing effects on concrete temperature. Noticeable differences in temperature in air persist only in boundary layers. The rest of the air volume has an almost constant temperature.

As geometry and boundary conditions are symmetric, both temperature and heat flux fields were symmetric.

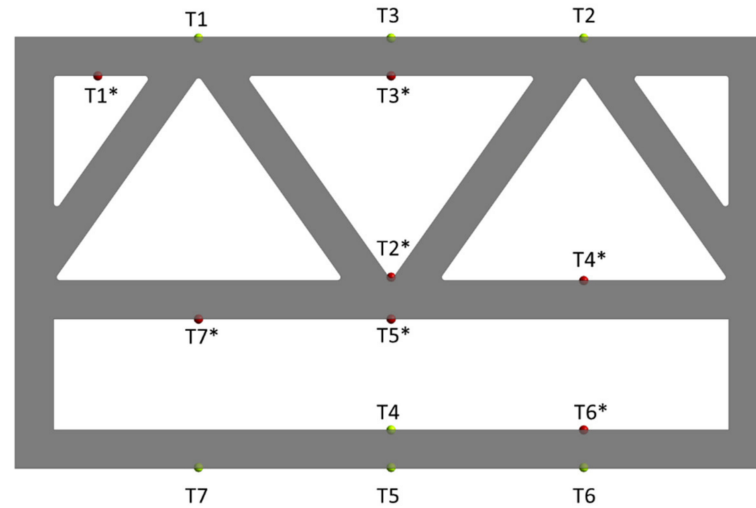
The thermal transmittance  $U$ -value is calculated by the formula:

$$U = \frac{\langle q \rangle}{\Delta T} \quad (4)$$

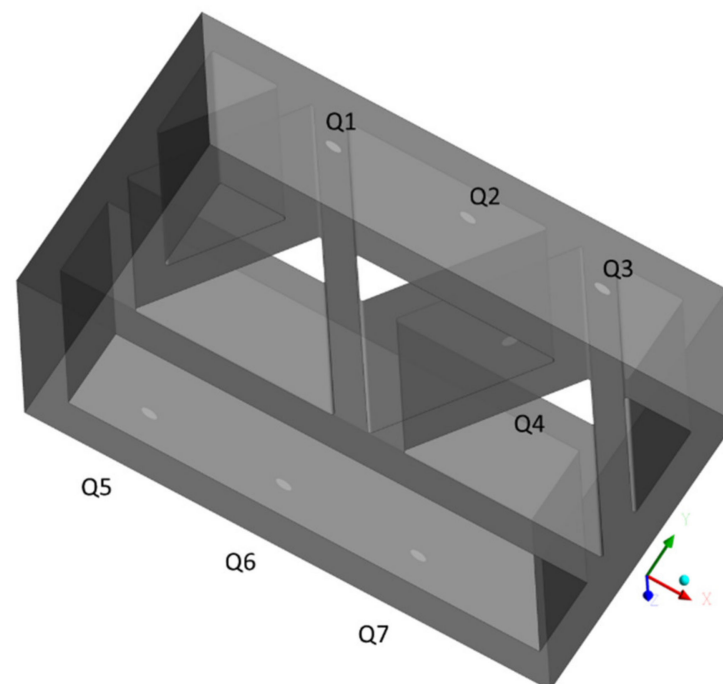
where  $\Delta T$ ,  $^{\circ}\text{C}$ , is temperature difference over construction and  $\langle q \rangle$ ,  $\text{W/m}^2$ , is the average heat flux through the construction  $U$ -value,  $1.18\text{ W/m}^2\cdot^{\circ}\text{C}$ .

### 3.1.4. Verification and Validation of CFD Simulations

Several experiments to computation in 14 points for temperature and 7 points for heat flux are compared. Figure 4b shows the position of the experimental sensor. Figures 13 and 14 show the numerical sensors' positions.



**Figure 13.** Numerical temperature sensors' positions ( $T_1$ – $T_7$  are temperature measurement sensors,  $T_{1^*}$ – $T_{7^*}$  are additional sensors for temperature measurement).



**Figure 14.** Numerical heat flux sensors' positions.

All obtained data are put into tables for easier comparison (Tables 4–6, where Exp1–Exp3 are data from the steady part of experiments 1–3, Comp represents computational data values, and Diff1–Diff3 is the difference between the corresponding experiment and computational data in percentages). The average temperature difference is 5% and the average heat flux difference is 30%. The heat flux difference is bigger because of the bigger uncertainty in the measurement of heat flux in the experiment.

**Table 4.** Temperature values.

| Sensor No. | Temperature T, °C |        |       |         |       |       |       |
|------------|-------------------|--------|-------|---------|-------|-------|-------|
|            | Exp1              | Exp2   | Exp3  | Comp    | Diff1 | Diff2 | Diff3 |
| 1          | −22.14            | −22.43 | −22.5 | −21.800 | 1.6%  | 2.9%  | 3.0%  |
| 2          | −21.27            | −21.50 | −22   | −21.800 | 2.5%  | 1.4%  | 0.9%  |
| 3          | −20.92            | −21.34 | −21.5 | −21.880 | 4.5%  | 2.5%  | 1.9%  |
| 4          | 15.07             | 15.04  | 14.81 | 15.820  | 4.9%  | 5.0%  | 6.6%  |
| 5          | 20.50             | 20.45  | 20.41 | 19.960  | 2.7%  | 2.4%  | 2.2%  |
| 6          | 19.88             | 20.23  | 20.18 | 19.960  | 0.4%  | 1.4%  | 1.1%  |
| 7          | 20.49             | 20.39  | 20.34 | 19.960  | 2.6%  | 2.1%  | 1.9%  |

**Table 5.** Temperature values.

| Sensor No. | Temperature T, °C |        |       |         |        |        |        |
|------------|-------------------|--------|-------|---------|--------|--------|--------|
|            | Exp1              | Exp2   | Exp3  | Comp    | Diff1  | Diff2  | Diff3  |
| 1          | −11.82            | −11.34 | −11.1 | −11.020 | 7.0%   | 2.8%   | 0.7%   |
| 2          | 1.21              | 0.04   | −0.33 | 0.19    | 146.0% | 131.7% | 743.2% |
| 3          | −14.23            | −15.30 | −15.6 | −15.000 | 5.3%   | 2.0%   | 3.9%   |
| 4          | 3.63              | 3.08   | 2.482 | 3.889   | 6.8%   | 23.1%  | 44.2%  |
| 5          | 8.28              | 7.58   | 7.322 | 7.947   | 4.1%   | 4.7%   | 8.2%   |
| 6          | 14.56             | 14.66  | 14.4  | 15.630  | 7.1%   | 6.4%   | 8.2%   |
| 7          | 9.16              | 8.46   | 8.307 | 8.568   | 6.7%   | 1.2%   | 3.1%   |

**Table 6.** Average heat flux.

| Sensor No. | Average Heat Flux, W/m <sup>2</sup> |       |       |       |       |       |       |
|------------|-------------------------------------|-------|-------|-------|-------|-------|-------|
|            | Exp1                                | Exp2  | Exp3  | Comp  | Diff1 | Diff2 | Diff3 |
| 1          | 48.57                               | 44.11 | 43.59 | 72.33 | 39.3% | 48.5% | 49.6% |
| 2          | 77.40                               | 71.57 | 72.45 | 72.51 | 6.5%  | 1.3%  | 0.1%  |
| 3          | 26.24                               | 24.46 | 23.52 | 30.88 | 16.2% | 23.2% | 27.0% |
| 4          | 18.32                               | 22.82 | 22.16 | 23.16 | 23.3% | 1.5%  | 4.4%  |
| 5          | 23.50                               | 18.78 | 19.07 | 39.88 | 51.7% | 71.9% | 70.6% |
| 6          | 27.46                               | 19.25 | 19.42 | 40.10 | 37.4% | 70.3% | 69.5% |
| 7          | 30.46                               | 24.53 | 25.35 | 40.10 | 27.3% | 48.2% | 45.1% |

As local temperature differences between experiment and computation are less than 10%, the computational model is assumed to be correct, so one can use this model to obtain the integral characteristics of U-values.

### 3.2. CFD Simulation of 3D-Printed Constructions with Different Configurations

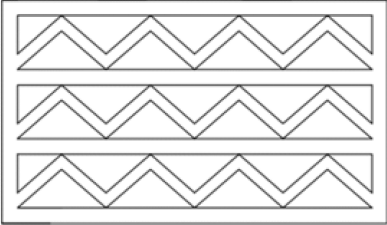
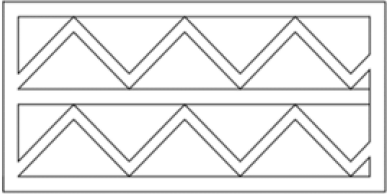
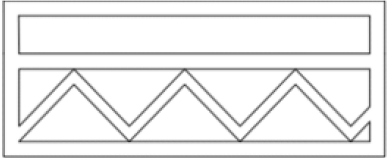
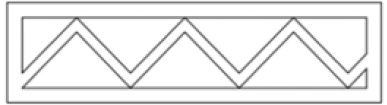
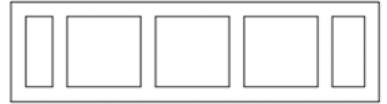


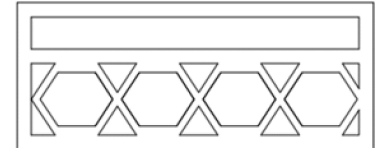
A validated numerical model of the process was obtained. This model can be used for other computations. Several computations with the same boundary conditions and computational methods but with different geometries were applied.  $U_e$ , W/m<sup>2</sup>·°C, in Tables 7 and 8 is the coefficient obtained with empirical formulas,  $U_c$ , W/m<sup>2</sup>·°C, is obtained from validated CFD simulation. Table 8 shows the results with the insulation layer. All calculations were made in the Ansys Fluent software package.

The convection can add some heat resistance compared to the empirical approach (as it was in geometries 1–3 and 8) and make it not better (as it was in geometries 4–7). Convection works better for more uneven cavern distributions.

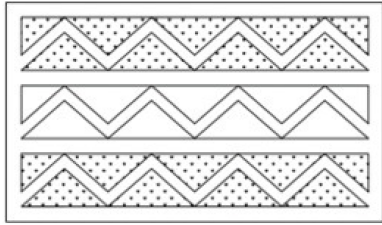
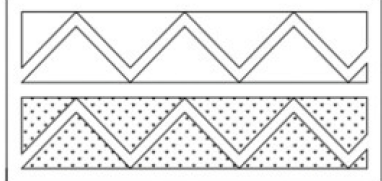
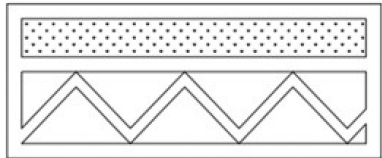
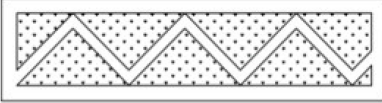

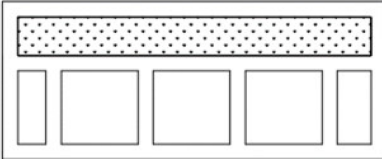
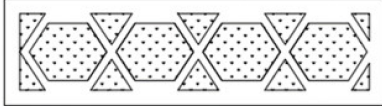
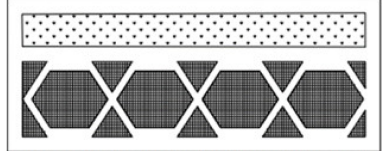
Empirical formulas give lower U-values and are unacceptable for engineering purposes for variants with insulation.



**Table 7.** Thermal transmittance U-values of 3D-printed constructions with different configurations.

| Characteristic | Construction Cross-Section View   | $U_e, \text{W/m}^2 \cdot ^\circ\text{C}$ | $U_c, \text{W/m}^2 \cdot ^\circ\text{C}$ |
|----------------|---|--|--|
| 1              |    | 1.03                                     | 0.89                                     |
| 2              |    | 1.37                                     | 1.05                                     |
| 3              |    | 1.52                                     | 1.15                                     |
| 4              |   | 2.13                                     | 2.00                                     |
| 5              |  | 2.38                                     | 3.03                                     |
| 6              |  | 1.52                                     | 1.59                                     |
| 7              |  | 2.08                                     | 2.04                                     |
| 8              |  | 1.49                                     | 1.25                                     |

**Table 8.** Thermal transmittance U-values of 3D-printed constructions with different configurations and types of insulation.

| Characteristic | Construction Cross-Section View   | $U_e, \text{W/m}^2 \cdot ^\circ\text{C}$ | $U_i, \text{W/m}^2 \cdot ^\circ\text{C}$ |
|----------------|---|--|--|
| 1              |    | 0.33                                     | 0.48                                     |
| 2              |    | 0.33                                     | 0.66                                     |
| 3              |   | 0.28                                     | 0.78                                     |
| 4              |  | 0.36                                     | 1.12                                     |
| 5              |  | 1.10                                     | 1.10                                     |
| 6              |  | 0.40                                     | 0.73                                     |
| 7              |  | 0.37                                     | 1.03                                     |
| 8              |  | 0.31                                     | 1.19                                     |

### 3.3. Energy Modeling Building with 3D-Printed Walls

The annual consumption of energy for heating is calculated using the following formula:

$$Q_{enc.str.}^{annual} = 0.024 \cdot (t_{int} - t_{ext}) \cdot z_{ht} \cdot U \cdot n \quad (5)$$

Here, 0.024 is a conversion factor of heat energy losses through external enclosing structures from  $\text{W} \cdot \text{day}$  to  $\text{kW} \cdot \text{h}$  (1 day = 24 h, 1 W = 0.001 kW, 1  $\text{W} \cdot \text{day}$  = 0.024  $\text{kW} \cdot \text{h}$ ).

$n$  is a coefficient that takes into account the dependence of the position of the external enclosing structure in relation to the outside air. It reduces the temperature difference for enclosing structures if they are not in direct contact with the outside air (for example, if there is a technical underground). All enclosing structures of the cottage are in contact with air; therefore,  $n = 1$ .

$(t_{\text{int}} - t_{\text{ext}}) \cdot z_{ht}$  in Formula (5) is called Heating Season Degree-Day, HSDD. It is a particular parameter. The HSDD characterizes the severity of winter in a region (the higher the HSDD, the colder it is). Without taking into account this parameter, it is impossible to compare the levels of energy efficiency of constructions built in different climatic regions. However, the methods for determining HSDD in other countries are not the same. The HSDD for Saint Petersburg (Russian Federation; its climatic zone according to the Köppen–Geiger climate classification is a humid continental climate with warm summers, Dfb [33]) is 4473.2 °C·day.

$U$  is the coefficient of heat transmission,  $\text{W}/\text{m}^2 \cdot ^\circ\text{C}$ .

The influence of different enclosing structures on the annual consumption of thermal energy is considered in the example of a cottage in Saint Petersburg (Figures 15–17).

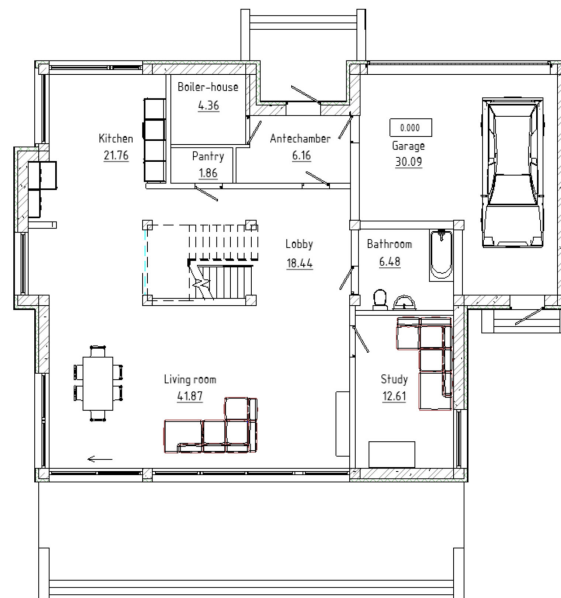


Figure 15. Plan of the first floor.

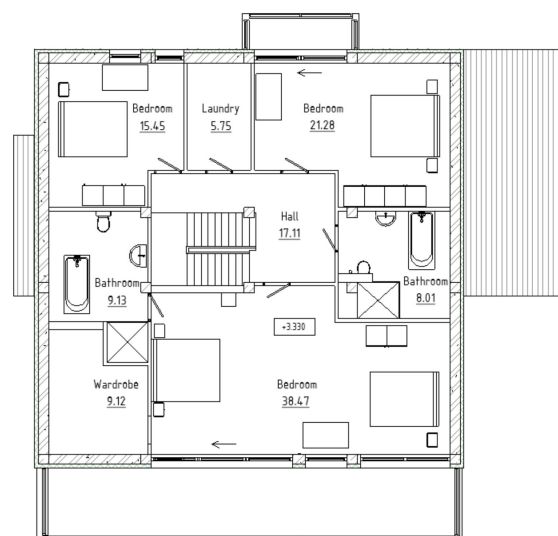
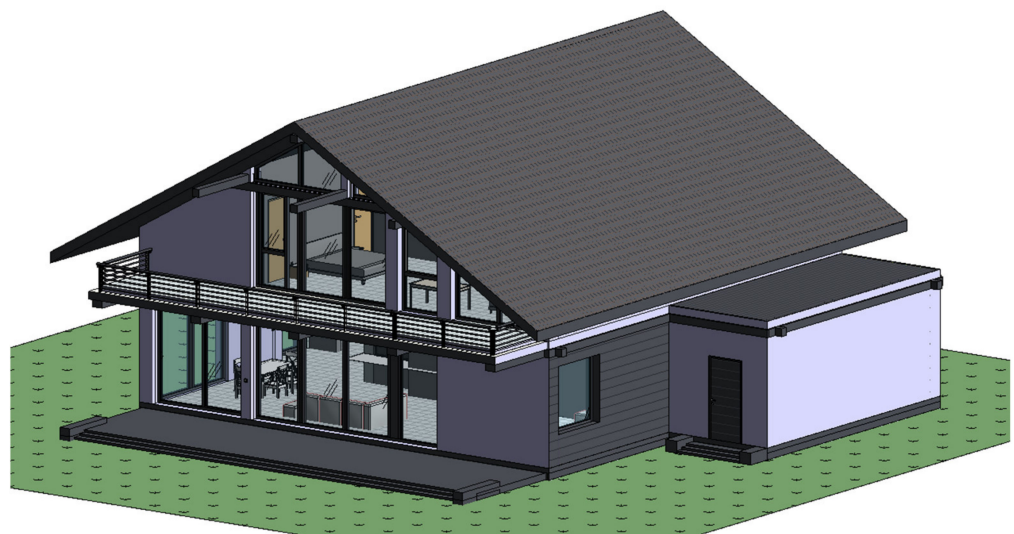


Figure 16. Plan of the second floor.



**Figure 17.** Three-dimensional view of the building.

The geometric and technical parameters for the calculation are shown in Table 9.

**Table 9.** Geometric and technical parameters for the calculation.

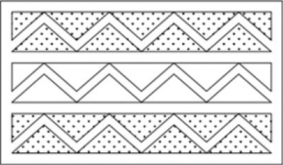
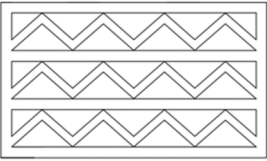
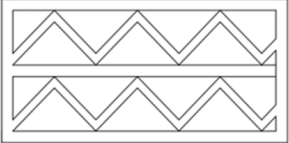
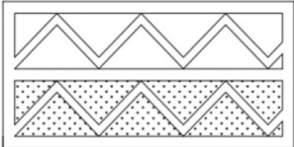
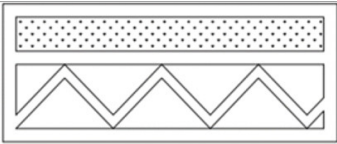
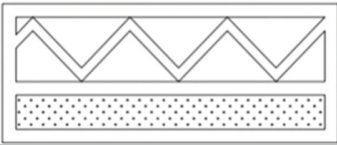

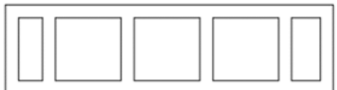

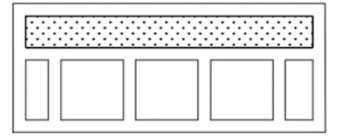

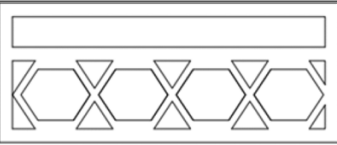
| Type of Enclosing Structure   | Construction Area, $A_i$ , m <sup>2</sup> | The Coefficient of Heat Transmission, $U$ , W/m <sup>2</sup> ·°C |
|---|---|--|
| Roof  | 264.45                                    | 0.22   |
| Stained-glass panels and balcony doors  | 89.28                                     | 1.33   |
| External entrance doors   | 16.88                                     | 1.11   |
| Foundation slab and floor   | 211                                       | 0.23   |
| The classic external enclosing structure  | Type of external enclosing structure      |  |
| Design No. 1, Option No. 1  | 182.23                                    | 0.21   |
|  | 182.23                                    | 0.64   |
| Design No. 1, Option No. 2  | 182.23                                    | 0.72   |
|  | 182.23                                    | 0.72   |
| Design No. 2, Option No. 1  | 182.23                                    | 1.05   |
|  | 182.23                                    | 1.05   |
| Design No. 2, Option No. 2  | 182.23                                    | 0.66   |
|  | 182.23                                    | 0.66   |

Table 9. Cont.

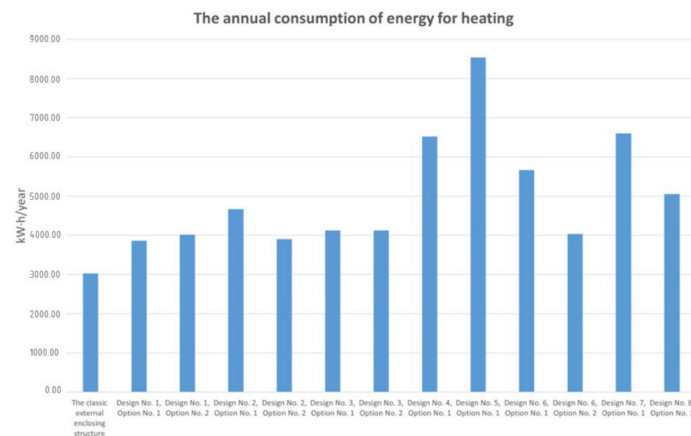
| Type of Enclosing Structure   | Construction Area, $A_i$ , m <sup>2</sup> | The Coefficient of Heat Transmission, $U$ , W/m <sup>2</sup> ·°C |
|---|---|--|
| Design No. 3, Option No. 1<br>   | 182.23                                    | 0.78   |
| Design No. 3, Option No. 2<br>   | 182.23                                    | 0.78   |
| Design No. 4, Option No. 1<br>   | 182.23                                    | 2  |
| Design No. 5, Option No. 1<br>  | 182.23                                    | 3.03   |
| Design No. 6, Option No. 1<br> | 182.23                                    | 1.56   |
| Design No. 6, Option No. 2<br> | 182.23                                    | 0.73   |
| Design No. 7, Option No. 1<br> | 182.23                                    | 2.04   |
| Design No. 8, Option No. 1<br> | 182.23                                    | 1.25   |

A classic wall structure consists of aerated concrete of 300 mm, insulation of 100 mm, and plaster of 5 mm.

Other wall structures are made by the additive method.

Figure 18 shows a graph illustrating the annual consumption of thermal energy of the 3D-printed building with different configurations of constructions.





**Figure 18.** The annual consumption of energy for heating.

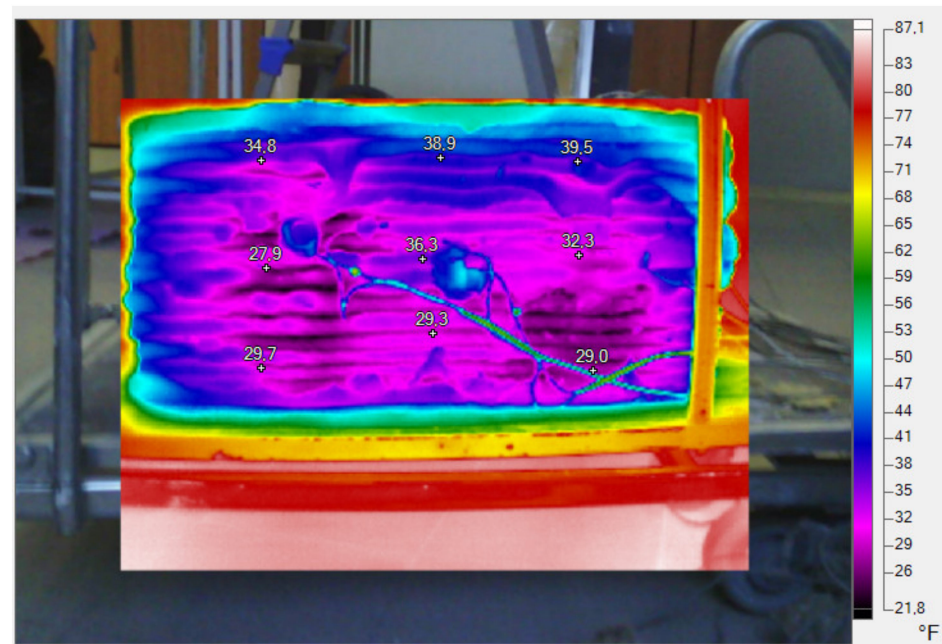
The annual energy consumption of the 3D-printed building with different construction configurations is between 3026 and 8536 kW·h per year.

According to the calculations, the classic wall structure turn out to be better in use. Design No. 1 (Option No. 1) and Design No. 2 (Option No. 2) are the most rational between proposed constructions. With further improvements, these designs will be able to work at the classical level and even be better.

Design No. 5 (Option No. 1) is the leader according to the annual energy consumption for heating the building. From the point of view of thermal engineering, this construction is the weakest. In the future, more heat will leave the room through it.

### 3.4. Thermal Imaging Results

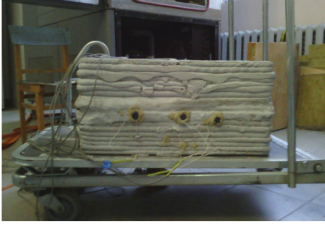


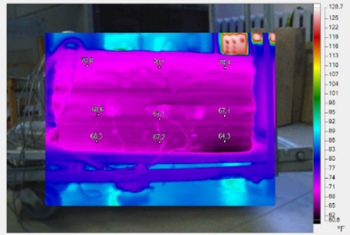
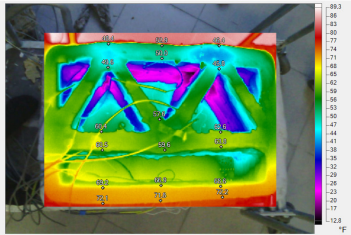
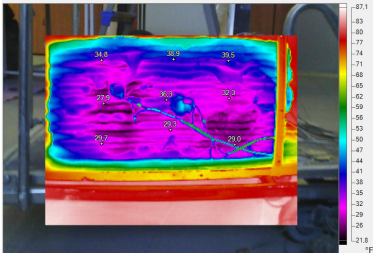
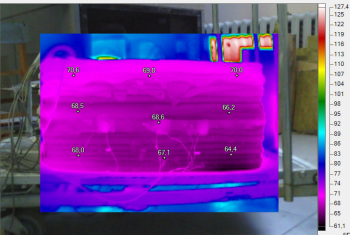
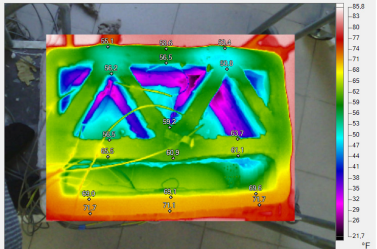
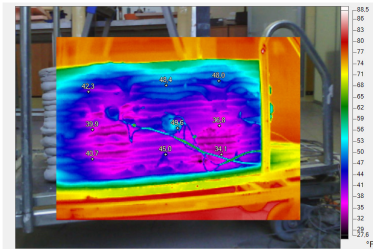
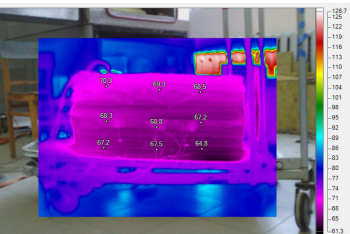
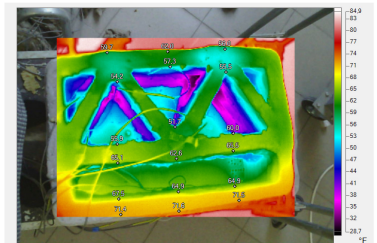
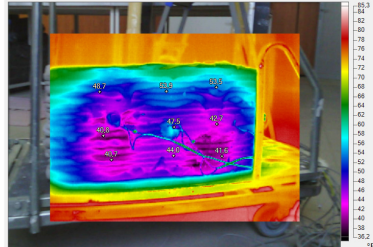
The study of thermal inhomogeneity is carried out by a non-destructive method using thermal imaging (Figure 19). The equipment used is Fluke TiS60+ Thermal Imager (Fluke Corporation, Everett, WA, USA; manufactured by Fluke Corporation, Everett, WA, USA).



**Figure 19.** Thermal imaging of 3D-printed wall.

The frequency of filming is 20 min. Table 10 presents the results.

**Table 10.** Thermal imaging results.

| Front of the Panel  | Top View of the Panel   | Back of the Panel   |
|---|---|---|
|    |    |    |
|    |    |    |
|   |   |   |
|  |  |  |

After removing the additive wall structure from the climatic chambers, it was examined with a thermal imager. The wall which was in the climatic chamber with a positive temperature gradually cooled down. On the contrary, the wall which was in the chamber with an imitation of the street began to heat up and gradually approached room temperature. At the same moment, the temperatures on the plane of the outer face differed. Structural ribs caused different temperatures on the outer surface to adjoin it from the inside, creating thermal inhomogeneity. The influence of non-uniform temperature distribution over the surface cannot be accurately considered for calculating U-values, only empirical formulas. It is necessary to carry out mathematical modeling for a specific design, considering its features.

Different surface temperatures require further study of inhomogeneities, thermal inclusions for structures developed using additive technologies, for the thermophysical properties of these structures.

#### 4. Conclusions

This research aimed to develop energy-efficient 3D-printed enclosing structures. The most used 3D-printed enclosing structural configurations were analyzed. New types of

configurations of 3D-printed enclosing structures were also proposed and analyzed. For the first time, a study was carried out on a structure made by 3D printing in climatic chambers with measurements of temperature and heat fluxes inside and outside the structure. Mesh-based finite volume ANSYS CFX was employed for the numerical simulation of heat and mass transfer in enclosing structures. Energy modeling of the building with 3D-printed enclosing structures with different construction configurations, energy consumption analysis, was conducted. The obtained results draw the following conclusions.

1. The time of temperature drop in the experimental sample of 3D-printed enclosing structure was determined. The temperature in a cold chamber,  $T_{\text{cold}} = -24\text{ }^{\circ}\text{C}$ , is dialed within 40 min from the start. For the first 120 min after the start, there is a precipitate drop in the temperature at the sides,  $\delta = 0\text{ mm}$  and  $\delta = 35\text{ mm}$ . The temperature drop occurs mainly inside the structure ( $\delta = 185\text{ mm}$ ,  $\delta = 255\text{ mm}$ ). After that, the time interval for comparing isotherms is equally more than two hours.
2. The CFD modeling of the 3D-printed enclosing structures was also completed. For the basic construction (basic for an experimental sample of 3D-printed enclosing structure), air is hotter on the upper part of the construction than the concrete lintel in the middle, but on the lower part, the air is colder than the lintel. The local temperature difference between concrete and air is around  $15\text{ }^{\circ}\text{C}$ .
3. The temperature isoline in the 3D-printed enclosing structure becomes more curved while moving the construction's center from either the hot or cold side. The temperature difference between the lower and the upper sides in the center of the 3D-printed enclosing structure side face is about  $5\text{ }^{\circ}\text{C}$ .
4. The heat flux through the solid parts of 3D-printed enclosing structures is severely higher (up to  $2\times$ ) than the heat flux through the air parts of the structures. The convection also influences heat flux distribution on surfaces. If the temperature gradients change because of convection, the heat flux changes (from  $100$  to  $70\text{ W/m}^2$ ) along the vertical coordinate.
5. There is one rectangular cavity, two hot triangle cavities, and three cold rectangular cavities. All cavities except small triangle ones seem to have stabilizing effects on concrete temperature. Noticeable differences in air temperature persist only in boundary layers. The rest of the air volume has an almost constant temperature. The average heat flux through the construction U-value is  $1.18$ .
6. The CFD simulation of 3D-printed enclosing structures with different configurations was obtained. Convection in the 3D-printed enclosing structures can add some heat resistance (Table 7) compared to the empirical approach (as it was in geometries 1–3 and 8) and make it not better (as it was in geometries 4–7). Convection works better for more uneven cavern distributions. Empirical formulas give lower U-values, which are unacceptable for engineering purposes for variants with insulation.
7. Energy modeling of the building with 3D-printed enclosing structures with different construction configurations was conducted. The annual energy consumption of the 3D-printed building with different construction configurations of 3D-printed enclosing structures is between  $3026$  and  $8536\text{ kW}\cdot\text{h}$  per year.
8. Thermal imaging results showed the presence of surface irregularities. These thermal inclusions require further research of inhomogeneities, thermal inclusions for structures developed by additive technologies, on the thermal properties of these structures.

**Author Contributions:** Conceptualization: D.N., E.K., V.O. and S.K.; methodology: T.M. and D.Z.; software: E.K.; validation: S.K. and E.K.; formal analysis: I.V.; investigation: T.M., D.Z., I.V., D.A., V.O. and E.K.; resources: V.O.; data curation: S.K.; writing—original draft preparation: D.A.; writing—review and editing: D.A. and D.N.; visualization: I.V. and E.K.; supervision: D.N.; project administration: V.O.; funding acquisition: D.N. All authors have read and agreed to the published version of the manuscript.

**Funding:** This work is supported by the Russian Science Foundation under grant 21-79-10283, date 29 July 2021, <https://rscf.ru/project/21-79-10283/> (accessed date 5 June 2022).



**Institutional Review Board Statement:** Not applicable.

**Informed Consent Statement:** Not applicable.

**Data Availability Statement:** Not applicable.

**Acknowledgments:** The authors would like to thank Nikolai Ivanovich Vatin, Peter the Great St. Petersburg Polytechnic University, St. Petersburg, Russia, for valuable and profound comments and «GidrolzolGroup» company (St. Petersburg, Russia) for help with the experiment.

**Conflicts of Interest:** The authors declare no conflict of interest.

## References

1. Suntharalingam, T.; Gatheeshgar, P.; Upasiri, I.; Poologanathan, K.; Nagaratnam, B.; Rajanayagam, H.; Navaratnam, S. Numerical Study of Fire and Energy Performance of Innovative Light-Weight 3d Printed Concrete Wall Configurations in Modular Building System. *Sustainability* **2021**, *13*, 2314. [\[CrossRef\]](#)
2. He, Y.; Zhang, Y.; Zhang, C.; Zhou, H. Energy-Saving Potential of 3D Printed Concrete Building with Integrated Living Wall. *Energy Build.* **2020**, *222*, 110110. [\[CrossRef\]](#)
3. Yang, S.; Wi, S.; Park, J.H.; Cho, H.M.; Kim, S. Novel Proposal to Overcome Insulation Limitations Due to Nonlinear Structures Using 3D Printing: Hybrid Heat-Storage System. *Energy Build.* **2019**, *197*, 177–187. [\[CrossRef\]](#)
4. Robati, M.; McCarthy, T.J.; Kokogiannakis, G. Incorporating Environmental Evaluation and Thermal Properties of Concrete Mix Designs. *Constr. Build. Mater.* **2016**, *128*, 422–435. [\[CrossRef\]](#)
5. Prasittisopin, L.; Pongpaisanseree, K.; Jiramarootapong, P.; Snguanyat, C. *Thermal and Sound Insulation of Large-Scale 3D Extrusion Printing Wall Panel*; Springer: Cham, Switzerland, 2020; Volume 28, pp. 1174–1182. [\[CrossRef\]](#)
6. Alkhalidi, A.; Hatuqay, D. Energy Efficient 3D Printed Buildings: Material and Techniques Selection Worldwide Study. *J. Build. Eng.* **2020**, *30*, 101286. [\[CrossRef\]](#)
7. González-Torres, M.; Pérez-Lombard, L.; Coronel, J.F.; Maestre, I.R.; Yan, D. A Review on Buildings Energy Information: Trends, End-Uses, Fuels and Drivers. *Energy Rep.* **2022**, *8*, 626–637. [\[CrossRef\]](#)
8. Marais, H.; Christen, H.; Cho, S.; de Villiers, W.; van Zijl, G. Computational Assessment of Thermal Performance of 3D Printed Concrete Wall Structures with Cavities. *J. Build. Eng.* **2021**, *41*, 102431. [\[CrossRef\]](#)
9. Thakur, N.; Prasath Kumar, V.R.; Balasubramanian, M. Comparative Energy Audit of Building Models Using BIM for the Sustainable Development. *J. Adv. Res. Dyn. Control Syst.* **2018**, *10*, 986–992.
10. Singh, P.; Sadhu, A. Multicomponent Energy Assessment of Buildings Using Building Information Modeling. *Sustain. Cities Soc.* **2019**, *49*, 101603. [\[CrossRef\]](#)
11. Ajayi, S.O.; Oyedele, L.O.; Ilori, O.M. Changing Significance of Embodied Energy: A Comparative Study of Material Specifications and Building Energy Sources. *J. Build. Eng.* **2019**, *23*, 324–333. [\[CrossRef\]](#)
12. Olanrewaju, S.D.; Adetunji, O.S.; Ogundepo, T.M. Achieving Energy Efficient Building through Energy Performance Analysis of Building Envelope in Student Housing. *J. Phys. Conf. Ser.* **2019**, *1378*, 042023. [\[CrossRef\]](#)
13. Bhamare, D.K.; Rathod, M.K.; Banerjee, J. Numerical Model for Evaluating Thermal Performance of Residential Building Roof Integrated with Inclined Phase Change Material (PCM) Layer. *J. Build. Eng.* **2020**, *28*, 101018. [\[CrossRef\]](#)
14. Shen, S.; Kanbur, B.B.; Zhou, Y.; Duan, F. Thermal and Mechanical Assessments of the 3D-Printed Conformal Cooling Channels: Computational Analysis and Multi-Objective Optimization. *J. Mater. Eng. Perform.* **2020**, *29*, 8261–8270. [\[CrossRef\]](#)
15. Kanbur, B.B.; Shen, S.; Zhou, Y.; Duan, F. Thermal and Mechanical Simulations of the Lattice Structures in the Conformal Cooling Cavities for 3D Printed Injection Molds. *Mater. Today Proc.* **2019**, *28*, 379–383. [\[CrossRef\]](#)
16. Khan, S.A.; Koç, M.; Al-Ghamdi, S.G. Sustainability Assessment, Potentials and Challenges of 3D Printed Concrete Structures: A Systematic Review for Built Environmental Applications. *J. Clean. Prod.* **2021**, *303*, 127027. [\[CrossRef\]](#)
17. Amran, M.; Abdelgader, H.S.; Onaizi, A.M.; Fediuk, R.; Ozbakkaloglu, T.; Rashid, R.S.M.; Murali, G. 3D-Printable Alkali-Activated Concretes for Building Applications: A Critical Review. *Constr. Build. Mater.* **2022**, *319*, 126126. [\[CrossRef\]](#)
18. Pan, Y.; Zhang, Y.; Zhang, D.; Song, Y. 3D Printing in Construction: State of the Art and Applications. *Int. J. Adv. Manuf. Technol.* **2021**, *115*, 1329–1348. [\[CrossRef\]](#)
19. Craveiro, F.; Bartolo, H.M.; Gale, A.; Duarte, J.P.; Bartolo, P.J. A Design Tool for Resource-Efficient Fabrication of 3d-Graded Structural Building Components Using Additive Manufacturing. *Autom. Constr.* **2017**, *82*, 75–83. [\[CrossRef\]](#)
20. Harmati, N.; Jakšić, Ž.; Vatin, N. Energy Consumption Modelling via Heat Balance Method for Energy Performance of a Building. *Procedia Eng.* **2015**, *117*, 786–794. [\[CrossRef\]](#)
21. Lee, Y.H.; Chua, N.; Amran, M.; Lee, Y.Y.; Kueh, A.B.H.; Fediuk, R.; Vatin, N.; Vasilev, Y. Thermal Performance of Structural Lightweight Concrete Composites for Potential Energy Saving. *Crystals* **2021**, *11*, 461. [\[CrossRef\]](#)
22. Klyuev, S.V.; Klyuev, A.V.; Vatin, N.I.; Shorstova, E.S. *Technology of 3-d Printing of Fiber Reinforced Mixtures*; Springer: Cham, Switzerland, 2021; Volume 141, pp. 224–230. [\[CrossRef\]](#)
23. Nair, A.; Aditya, S.D.; Adarsh, R.N.; Nandan, M.; Dharek, M.S.; Sreedhara, B.M.; Prashant, S.C.; Sreekeesha, K.S. Additive Manufacturing of Concrete: Challenges and Opportunities. *IOP Conf. Ser. Mater. Sci. Eng.* **2020**, *814*, 012022. [\[CrossRef\]](#)

24. Nazarian, S.; Duarte, J.P.; Bilén, S.G.; Memari, A.; Radlinska, A.; Meisel, N.; Hojati, M. Additive Manufacturing of Architectural Structures: An Interplay Between Materials, Systems, and Design. In *Sustainability and Automation in Smart Constructions. Advances in Science, Technology & Innovation*; Rodrigues, H., Gaspar, F., Fernandes, P., Mateus, A., Eds.; Springer: Cham, Switzerland, 2021; pp. 111–119. [[CrossRef](#)]
25. Buswell, R.A.; Leal de Silva, W.R.; Jones, S.Z.; Dirrenberger, J. 3D Printing Using Concrete Extrusion: A Roadmap for Research. *Cem. Concr. Res.* **2018**, *112*, 37–49. [[CrossRef](#)]
26. Dobrzyńska, E.; Kondej, D.; Kowalska, J.; Szewczyńska, M. State of the Art in Additive Manufacturing and Its Possible Chemical and Particle Hazards—Review. *Indoor Air* **2021**, *31*, 1733–1758. [[CrossRef](#)]
27. Gosselin, C.; Duballet, R.; Roux, P.; Gaudillière, N.; Dirrenberger, J.; Morel, P. Large-Scale 3D Printing of Ultra-High Performance Concrete—A New Processing Route for Architects and Builders. *Mater. Des.* **2016**, *100*, 102–109. [[CrossRef](#)]
28. Lowke, D.; Dini, E.; Perrot, A.; Weger, D.; Gehlen, C.; Dillenburger, B. Particle-Bed 3D Printing in Concrete Construction—Possibilities and Challenges. *Cem. Concr. Res.* **2018**, *112*, 50–65. [[CrossRef](#)]
29. Vatin, N.I.; Gorshkov, A.S.; Nemova, D.V. Energy Efficiency of Envelopes at Major Repairs. *Constr. Unique Build. Struct.* **2013**, *3*, 1–11.
30. Sergeev, V.; Vatin, N.; Kotov, E.; Nemova, D.; Khorobrov, S. Slug regime transitions in a two-phase flow in horizontal round pipe. cfd simulations. *Appl. Sci.* **2020**, *10*, 8739. [[CrossRef](#)]
31. Buswell, R.A.; Thorpe, A.; Soar, R.C.; Gibb, A.G.F. Design, Data and Process Issues for Mega-Scale Rapid Manufacturing Machines Used for Construction. *Autom. Constr.* **2008**, *17*, 923–929. [[CrossRef](#)]
32. Buswell, R.A.; Soar, R.C.; Gibb, A.G.F.; Thorpe, A. Freeform Construction: Mega-Scale Rapid Manufacturing for Construction. *Autom. Constr.* **2007**, *16*, 224–231. [[CrossRef](#)]
33. Saracoglu, A.; Sanli, D.U. Accuracy of GPS Positioning Concerning Köppen-Geiger Climate Classification. *Measurement* **2021**, *181*, 109629. [[CrossRef](#)]